Title

Linking water quality, fouling layer composition, and performance of reverse osmosis membranes

Authors

Landsman, Matthew R
Rongpipi, Sintu
Freychet, Guillaume
et al.

Publication Date

2023-08-01

DOI

10.1016/j.memsci.2023.121717

Peer reviewed

Linking Water Quality, Fouling Layer Composition, and Performance of Reverse Osmosis Membranes

Matthew R. Landsman[1,2], Sintu Rongpipi[2,3], Guillaume Freychet[4], Eliot Gann[5], Cherno Jaye[5], Desmond F. Lawler[1], Lynn E. Katz[1*], and Gregory M. Su[2,3*]

*co-corresponding authors: gsu@lbl.gov, 1 Cyclotron Road, Lawrence Berkeley National Laboratory, Berkeley, CA 94720; lynnkatz@mail.utexas.edu, 301 E Dean Keeton Street, ECJ 9.102H, University of Texas at Austin, Austin, TX 78712 United States

[1]Department of Civil, Architectural, and Environmental Engineering, University of Texas at Austin, Austin, TX 78712 United States

[2]Advanced Light Source, Lawrence Berkeley National Laboratory, Berkeley, CA 94720 United States

[3]Materials Sciences Division, Lawrence Berkeley National Laboratory, Berkeley, CA 92720 United States

[4]National Synchrotron Light Source II, Brookhaven National Laboratory, Upton, NY 11973 United States

[5]Materials Measurement Science Division, National Institute of Standards and Technology, Gaithersburg, MD 20899 United States

Resubmitted to *Journal of Membrane Science*

April 16, 2023

Abstract

Fouling of polyamide membranes during reverse osmosis (RO) is a major challenge for adopting membrane technologies to treat highly contaminated waters, especially those containing organic foulants (e.g., natural organic matter (NOM), polysaccharides) and dominant cations (e.g., sodium, magnesium, calcium). This work combines bench-scale membrane fouling experiments with detailed characterization of feedwater chemistry and fouling layer composition/morphology to reveal fundamental mechanisms of (in)organic fouling during RO. Divalent cations are shown to promote fouling by hydrophobic NOM containing aromatic and carboxyl groups, while NOM fouling in the presence of a monovalent cation, sodium, occurs by smaller fulvic acids containing larger fractions of carboxyl groups and other oxygen-rich moieties. Calcium-carboxyl bridging occurs in solution and near the membrane surface to induce NOM aggregation on nanometer length scales. In complex waters containing foulant mixtures, co-fouling by calcium-carboxyl bridging and $CaCO_3$ precipitation influence membrane performance at longer timeframes. However, the flux decline observed for the co-fouling mechanism was less significant than the sum of its parts, suggesting both synergistic and antagonistic fouling mechanisms should be considered in membrane design/operation. These results encourage the design of pretreatment processes to reduce concentrations of multivalent ions and hydrophobic NOM in RO feedwaters, and of membrane materials to limit attachment/deposition of aggregates to/on polyamide surfaces.

Keywords: polyamide, natural organic matter, calcium carbonate, resonant x-ray scattering, x-ray absorption spectroscopy

Hightlights

- Unique (in)organic (co-)fouling mechanisms are revealed via synchrotron techniques
- Ca^{2+} and Mg^{2+} promote significant fouling by aromatic+carboxyl containing organics
- Na^{+} promotes fouling by smaller, oxygen-rich organics that have less impact on flux
- X-ray scattering shows Ca^{2+}-bridged organic foulants aggregate at nm length scales
- Alginate fouling inhibits/slows the formation of $CaCO_3$ scales (calcite vs. vaterite)

Graphical Abstract

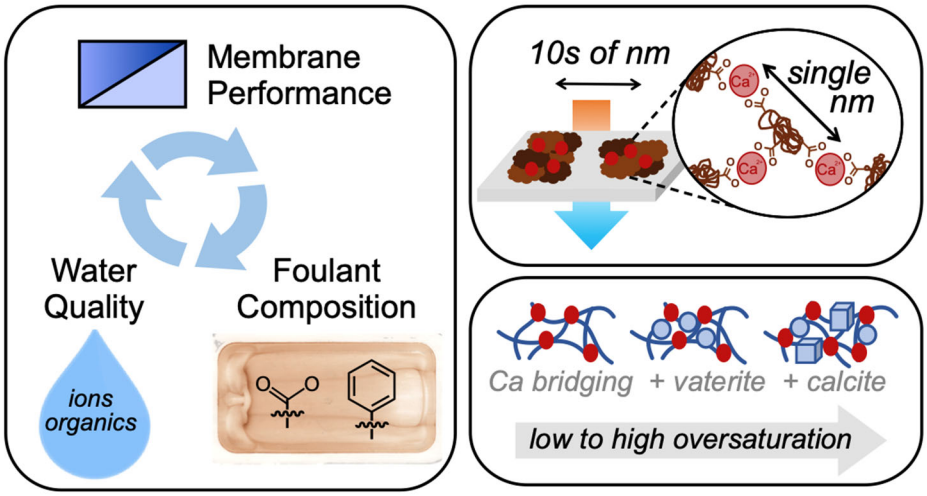

1. Introduction

Reverse osmosis (RO) is a prominent technology for removing dissolved contaminants during desalination and water reuse, but current RO processes are limited by the tendency for polyamide membranes to foul during operation [1–4]. Fouling is a widespread challenge to using membranes for water purification because the attachment/deposition of foulants, which include particles, (in)organic contaminants, and biological species, on membrane surfaces and in membrane pores increases the resistance to water permeation, raising the energy requirement for a given water recovery. Moreover, the development of foulant-rich interfaces near RO membrane surfaces influences interfacial interactions (e.g., concentration polarization, hydrogen bonding) that can decrease solute rejection [5–7]. While the macroscopic impacts of membrane fouling are well-documented and significant efforts are underway to design fouling-resistant materials/processes, significant gaps exist regarding the interplay of molecular-level fouling mechanisms and overall membrane performance [8–10]. This work presents a multimodal investigation of RO membrane fouling to provide experimental validation of well-documented and frequently-encountered fouling mechanisms and the interplay of synergistic/antagonistic mechanisms in complex waters.

RO membranes are especially prone to organic fouling by natural organic matter (NOM), proteins, polysaccharides, and soluble microbial products [11,12]. NOM – a general category of polydisperse organic molecules existing in the environment – contributes to fouling via adsorption to membrane surfaces and interactions with solute/membrane functional groups [13,14]. Carboxylic acids comprise most of the acidic functional groups on polyamide membrane surfaces and in the humic/fulvic acids present in NOM [15–17], rendering them negatively

charged in many waters since most carboxylic acids have a pK_a near 4.5 [18]. Cations screen the negative charge of organic functional groups and reduce the electrostatic repulsion of macromolecules to each other and to membrane surfaces, increasing fouling potential [19,20]. Additionally, multivalent cations form intermolecular bridges between carboxyl-containing compounds, which promotes supramolecular NOM aggregation and exacerbates fouling [20–22].

Reducing RO membrane fouling can be achieved through pretreatment (e.g., softening), membrane modifications (e.g., antifouling coatings), and/or changing operational parameters (e.g., pressure, crossflow rate, cleaning protocols) [2,12], but the optimal conditions for preventing NOM fouling depend on a complex interplay among membrane operation and water chemistry. Operating RO membranes at low crossflow rate and/or high permeate flux typically increases fouling [23,24]. Meanwhile, low pH and high ionic strength promote NOM coiling/aggregation and reduce electrostatic repulsion, which induces significant fouling [14,25,26]. Ion-specific effects must also be considered, and it is generally accepted that calcium bridging of carboxyl groups is more significant than magnesium bridging; such behavior is ascribed to the tightly-bound hydration shell of magnesium cations [20,22,27,28]. Finally, in waters containing inorganic scalants (e.g., $CaCO_3$, $CaSO_4$, silica) [29], synergistic interactions among foulants can increase fouling beyond the sum of the individual foulants [30,31]. In addition to foulant properties and water chemistry parameters, membrane physiochemical properties including surface chemistry, roughness, and swelling also impact the behavior of water and solutes at the membrane-water interface and contribute to membrane fouling [32–34].

Fouling studies traditionally rely on macroscopic membrane performance metrics (e.g., flux decline) and conventional characterization techniques (e.g., infrared spectroscopy, scanning

electron microscopy) to determine fouling mechanisms. Foulant-specific information can be difficult to extract/interpret using conventional techniques [35,36], requiring a combination of characterization techniques (i.e., a multimodal approach) that provide chemical and structural information across multiple length scales. Synchrotron-based spectroscopic and scattering techniques are promising tools for studying precipitation and fouling processes [36,37]; for example, Jun *et al.* [38] monitored mineral nucleation/growth near inorganic surfaces using x-ray scattering to reveal particle sizes and interfacial energies that could not be obtained using conventional methods. For complex foulants such as NOM, the development of characterization tools that give quantitative, spatial distributions of individual chemical species will significantly advance our understanding of – and in turn, our ability to model and design around – membrane fouling during RO.

The objective of this study is to reveal the underlying mechanisms of RO membrane fouling by organic foulants (NOM and alginate) in the presence of dominant cations (sodium, magnesium, and calcium) and a ubiquitous anion (carbonate). This research combines bench-scale membrane fouling experiments, water quality analyses, and fouling layer characterization via synchrotron spectroscopy/scattering to determine the contributions of specific foulant-foulant and foulant-membrane interactions to membrane performance decline. These results inform the design of membrane materials and treatment trains to minimize fouling.

2. Materials and Methods

2.1. Feedwater solutions

Initial fouling experiments were performed using a synthetic surface water containing NOM at 10 mg C/L, $NaHCO_3$ at 0.5 mmol/L (for pH control), and NaCl, $CaCl_2$, or $MgCl_2$ such that the ionic strength of the solution was 10 mmol/L. The goal of these experiments was to determine the (individual) contributions of major cations (Na^+, Mg^{2+}, Ca^{2+}) on NOM fouling. All inorganic salts were of ACS grade and purchased from Sigma Aldrich or Fisher Scientific. Two reference NOM samples – Suwannee River NOM (SNOM) (catalog number 2R101N) and Upper Mississippi River NOM (MNOM) (catalog number 1R110N) – were purchased from the International Humic Substances Society (St. Paul, MN, USA). Concentration and isolation processes for obtaining NOM from natural waters can impact composition. SNOM was concentrated from the raw water via RO and the concentrated NOM was desalted by cation exchange (Dowex 50Wx8, H^+ form), freeze dried, and homogenized [39]. Extraction of MNOM used similar protocols but electrodialysis (ED) was employed after RO to isolate NOM from the hard water rich in calcium and magnesium [40]. RO extraction of NOM not only extracts the hydrophobic and hydrophilic acids that are readily adsorbed during NOM isolation using Amberlite XAD resins but also other soluble organics, and SNOM extracted via RO has been shown to contain more polar aliphatic materials such as polysaccharides and polypeptides than the humic and fulvic acids isolated from the Suwannee River using Amberlite XAD resins [41].

In addition to the NOM fouling experiments, a set of RO experiments employed mixtures of sodium alginate (catalog number A2033, Sigma Aldrich), a model organic foulant with a high density of carboxyl groups (14.5 meq/g C, Table S1), and carbonate (CO_3^{2-}), a ubiquitous anion

142 that contributes to membrane scaling. The goal of these experiments was to determine the
143 influence of competing/synergistic fouling mechanisms. The synthetic feedwaters employed in
144 these experiments had an ionic strength of 100 mmol/L, a total calcium concentration of 10
145 mmol/L, an alginate concentration of 25 mg C/L, and total carbonate concentrations ranging
146 from 0.5 mmol/L to 8.6 mmol/L such that the feedwaters exhibited log(saturation index) (logSI)
147 values of calcite ($CaCO_3$) between 0.23 and 1.4 (Table S5).
148 Foulant stock solutions were filtered through 0.22 μm polyethersulfone filters (Pall
149 Corporation, Albany, NY, USA) to reflect the microfiltration/ultrafiltration pretreatment that is
150 typical of membrane-based water treatment trains that include RO. Filtration of NOM stock
151 solutions led to significant buildup of insoluble humin on the filters such that the NOM
152 molecules in the stock solutions employed herein favor relatively low molecular weight fractions
153 relative to studies in literature that employ unfiltered NOM solutions. Additional information on
154 the feedwaters/foulants is provided in Section S1.
155
156 *2.2. Bench-scale fouling experiments*
157 Membrane fouling experiments used a Sterlitech CF042D crossflow cell (Sterlitech,
158 Kent, WA, USA) and a variable-speed diaphragm pump (HydraCell, Wanner Engineering Inc.,
159 Minneapolis, MN, USA), as presented in our previous work [42,43]. All fouling experiments
160 were performed at a constant pressure of 2.76 MPa (400 psi, 27.6 bar) and a constant feedwater
161 crossflow velocity of 0.1 m/s. The pressure and crossflow rate used herein are higher and lower
162 than typical operating conditions, respectively, because these conditions enabled accelerated
163 fouling experiments in the bench-scale system. The retentate and permeate streams were

recirculated to a feed reservoir maintained at 25.0 °C ± 0.2 °C. The total volume of the system (i.e., the feed tank plus the tubing and the crossflow cell) was 2 L such that changes in the feedwater composition caused by fouling could be investigated. Relevant metadata of water chemistry (i.e., solution pH, temperature, and conductivity) and membrane operational (i.e., permeate flux and applied pressure) parameters were recorded using LabVIEW (National Instruments, Austin, TX, USA). The crossflow rate was recorded manually with a floating disc rotameter (King Instrument, Fresno, CA).

This research employed the FilmTec BW30 membrane (DuPont Water Solutions, Wilmington, DE, USA) for fouling studies. Some physiochemical properties of the BW30 membrane are presented and discussed in Section S2. Flat sheet membranes were pre-conditioned in 25 vol. % isopropyl alcohol (Sigma Aldrich) for 30 minutes and stored in DI water in the dark at 4 °C until use. Prior to a fouling experiment, a pristine BW30 membrane was conditioned by permeating DI water for one hour followed by flux stabilization using the background salt solution, which occurred within a few hours. Then, the pressure was removed, the foulant was added to the feedwater, and the pH was adjusted to 8.0 ± 0.1 to reflect typical water treatment processes. The pressure was then re-applied to initiate fouling. As described in Section S2, MATLAB (MathWorks, Natick, MA, USA) was used to calculate the volume of permeated water and the experiments were ended at 1000 L of permeate per m^2 of membrane surface for NOM fouling and 100 L/m^2 for alginate fouling. The end volume was lower for alginate fouling experiments compared to NOM fouling experiments because, with the higher concentrations of ions/foulants in alginate feedwaters, fouling occurred more rapidly. Additional information, including a summary table of the experiments, can be found in Section S2.

186 At the end of each experiment, fouled membranes were lightly rinsed with DI water to
187 remove constituents that were not attached to the membrane (i.e., non-foulants) and air-dried
188 overnight in a clean dish. Table 1 presents the subsequent techniques employed to characterize
189 the feedwaters and membranes; brief descriptions of the analyses are provided in Sections 2.3
190 and 2.4 and additional information is available in the Supplementary Materials. Note that control
191 experiments in which the background salt solutions (i.e., foulant feedwaters without organic
192 foulants) were treated led to insignificant fouling of the RO membranes.
193

Table 1. Summary of water quality and membrane fouling layer characterization techniques.

Measurement	Abbreviation	Information obtained
Water quality		
Dissolved organic carbon	DOC	Surrogate measure of NOM concentration in feedwater
Specific ultraviolet absorbance	$SUVA_{254}$	Surrogate measure of NOM hydrophobicity in feedwater
Inductively coupled plasma-Optical emission spectrometry	ICP-OES	Cation (Na^+, Mg^{2+}, Ca^{2+}) concentrations in feedwater
High performance size exclusion chromatography	HPSEC	NOM molecular weight distribution in feedwater
Membrane fouling layer		
Digestion + ICP-OES	-	Cation (Na^+, Mg^{2+}, Ca^{2+}) concentrations in fouling layers
Near edge x-ray absorption fine structure spectroscopy	NEXAFS spectroscopy	Chemical composition of fouling layers, performed at the C, O, Mg, and Ca K-edges and the Ca $L_{3,2}$-edge
Resonant soft x-ray scattering	RSoXS	Spatial distribution of foulants within fouling layers, performed at the Ca $L_{3,2}$-edge
Tender resonant x-ray scattering	TReXS	Spatial distribution of foulants within fouling layers, performed at the Ca K-edge
Wide angle x-ray scattering	WAXS	Crystal phases of inorganic scalants ($CaCO_3$) within fouling layers

2.3. Water quality analysis

Feedwater samples were collected at the beginning and end of NOM fouling experiments to study changes in the feedwater composition caused by fouling. Dissolved organic carbon (DOC) concentrations were determined using a total organic carbon analyzer (TOC-L CPH/CPN, Shimadzu, Kyoto, Japan) and cation concentrations were determined via inductively coupled plasma-optical emission spectrometry (ICP-OES) (Varian 710-ES, Agilent, Santa Clara, CA, USA). Ultraviolet (UV) absorbance spectra were collected using an Agilent 8453 UV-vis spectrometer and specific ultraviolet absorbance ($SUVA_{254}$) values were calculated as the ratio of UV absorbance at 254 nm to DOC concentration. $SUVA_{254}$ values are used as a surrogate measure of NOM hydrophobicity in solutions with the same NOM source [44]. High performance size exclusion chromatography (HPSEC) was employed to determine NOM molecular weight distributions in solution before and after fouling experiments. HPSEC was performed on a Dionex UltiMate 3000 UHPLC (Thermo Scientific) with a Protein-Pak 125 column (Waters Corporation, Milford, MA, USA) and a variable wavelength detector set to 224 nm, following the methods of McAdams *et al.* [45].

2.4. Membrane fouling layer characterization

2.4.1. Quantification of inorganic foulant densities

The density of inorganic cations in membrane fouling layers was quantified by microwave digesting membrane samples of known surface area and determining cation concentrations in the digested solutions via ICP-OES. Membrane coupons were cut out and digested in 10 mol/L nitric acid (trace metal grade, Thermo Scientific) on an ETHOS^{TM} UP

219 microwave digestion system (Milestone, Shelton, CT, USA). The polyester backing of the BW30
220 membrane was carefully removed before digesting the membrane coupon due to incomplete
221 digestion of the backing. The backing was then scanned using a flatbed scanner and the surface
222 area of the membrane coupon was determined in ImageJ [46]. Cation concentrations in the
223 digested solutions were converted to surface densities (mmol/m^2) via mass balance. Triplicate
224 measurements showed no evidence of gradients of inorganic cation concentrations along the
225 flowpath of the membrane. Digestion of the membranes that were used to treat the background
226 salt solutions showed insignificant (<0.1 mmol/m^2) concentrations of inorganic cations on the
227 RO membrane surfaces, and the subsequent characterization techniques also confirmed the
228 absence of quantifiable membrane fouling in systems without organic matter or high
229 concentrations of carbonate.
230
231 *2.4.2. X-ray absorption spectroscopy and resonant x-ray scattering*
232 Membrane samples were analyzed via *ex situ* near edge x-ray absorption fine structure
233 (NEXAFS) spectroscopy and resonant soft and tender x-ray scattering (RSoXS and TReXS,
234 respectively) at the National Synchrotron Light Source II (NSLS-II) (Brookhaven, NY, USA). X-
235 ray absorption spectroscopy is sensitive to chemical bonds, so NEXAFS measurements enabled
236 detailed characterization of the organic (i.e., carbon and oxygen) and inorganic (i.e., calcium and
237 magnesium) components of the fouling layers. RSoXS and TReXS combine the spatial
238 information (e.g., size, shape) obtained from x-ray scattering with the chemical sensitivity of
239 NEXAFS to probe the morphology/structure of samples across an elemental absorption edge

[47–49]. In this study, RSoXS and TReXS were utilized to investigate the distribution of calcium in NOM fouling layers.

NEXAFS/RSoXS measurements using soft x-rays with energies near the carbon (≈290 eV), oxygen (≈540 eV), and magnesium (≈1310 eV) K-edges and the calcium $L_{3,2}$-edge (≈350 eV) were performed at beamline SST-1 (7-ID-1) at NSLS-II [50]. Experiments using soft x-rays employed two geometries/detection modes: transmission, in which the entire thickness of the sample is penetrated, and partial electron yield (PEY), which is surface sensitive (i.e., probing depth of a few nm) [51]. Soft x-rays can only penetrate thin samples and the estimated attenuation length – which defines the depth into a material where the intensity of an x-ray is 1/e (≈37 %) of its value at the surface – of soft x-rays through a polyamide material is approximately 1 μm (Figure S10) [52]. Therefore, the free float method developed by Culp *et al.* [53] was used to isolate the ultrathin (≈100 nm) polyamide layer (and in some cases, a fouling layer) from the support layers of the BW30 membrane. The isolated polyamide(+fouling) layer was mounted on a silicon nitride window (Norcada, Edmonton, Alberta, Canada) for soft x-ray transmission NEXAFS and RSoXS measurements. PEY NEXAFS measurements only probe the top surface of samples, so extensive sample preparation was not necessary for these measurements.

TReXS and NEXAFS measurements near the calcium K-edge (≈4050 eV) were performed at the SMI beamline (12-ID) at NSLS-II in a transmission geometry and with fluorescence yield (FY) detection, respectively [54]. The estimated attenuation length of tender x-rays through a polyamide material is approximately 50 μm [52], so sample preparation for calcium K-edge NEXAFS/TReXS measurements involved carefully removing the polyester

backing of the RO membranes and mounting the remaining polyamide, fouling layer, and polysulfone support layer (≈50 μm thick) on a washer.

2.4.3. Wide-angle x-ray scattering

Membrane samples were analyzed via *ex situ* wide angle x-ray scattering (WAXS) at beamline 7.3.3 of the Advanced Light Source (ALS) (Berkeley, CA, USA) [55]. WAXS profiles were collected at a single energy, 10 keV, providing no resonance/chemical sensitivity, but the diffraction patterns were used to identify scalants in the fouling layers. Hard x-rays penetrate millimeter-thick samples (Figure S10) [52], so the same mounting procedure used for calcium K-edge measurements was employed for WAXS measurements.

3. Results and Discussion

3.1. Divalent cations promote fouling of high molecular weight NOM

The presence of divalent cations – especially calcium – in NOM feedwaters immediately promotes significant flux decline during RO (Figure 1A). Similar results have been reported by other researchers and are attributed to bridging of carboxyl groups in NOM by divalent cations [14,20,23,24]. In all cases, SNOM fouling is more significant than MNOM (Table S4); this difference is intriguing given the similar compositions of the NOM sources (Table S1). The general trends in this work are similar among the two NOM sources, so the results presented herein focus on SNOM, while MNOM is discussed in Section S4. Briefly, MNOM is shown to cause less significant membrane fouling because MNOM fouling layers contain larger fractions of hydrophilic (e.g., carboxyl) functional groups relative to SNOM fouling layers. These results

283 imply that molecules exhibiting similar fouling mechanisms can have varying impacts on
284 macroscopic fouling behavior depending on the physiochemical composition of the foulants.

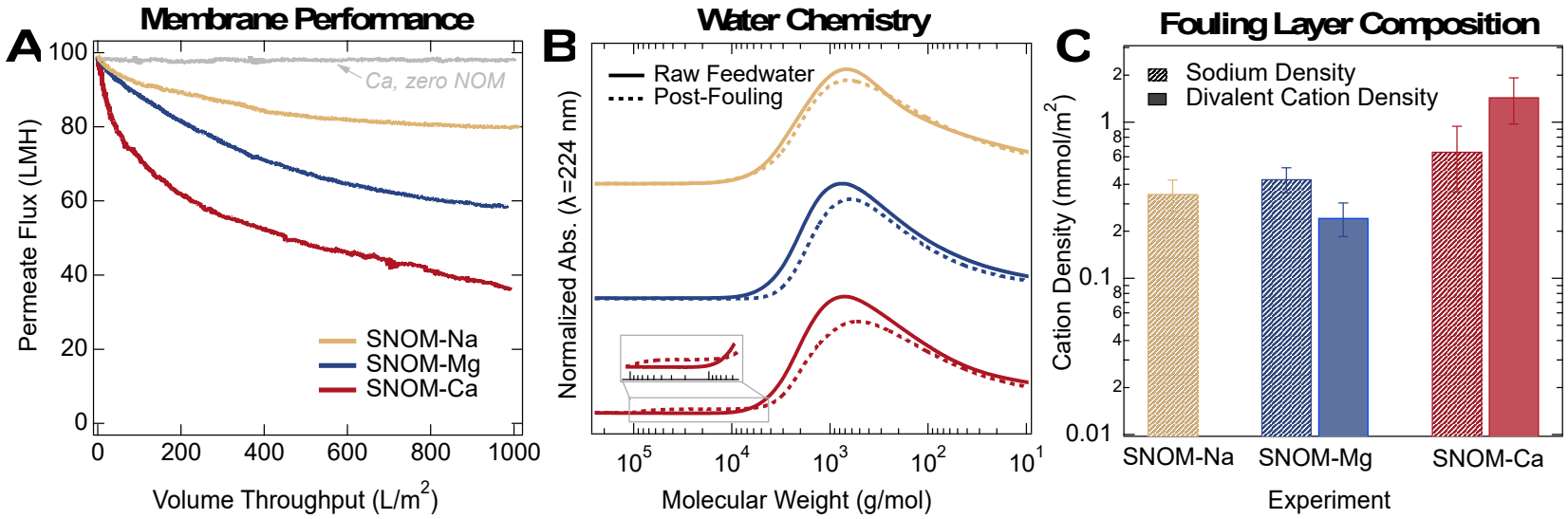

Figure 1. (A) Membrane flux decline during recirculating RO experiments shows significant NOM fouling in the presence of divalent cations, especially calcium. The grey trace confirms that no fouling occurs for feedwaters without NOM. (B) Size exclusion chromatographs of pre- and post-fouling feedwaters reveal a shift in solution-phase NOM molecular weights caused by RO membrane fouling, where divalent cations promote fouling by high molecular weight NOM and calcium aggregates NOM in solution (see inset). (C) Quantification of inorganic foulants on RO membrane surfaces confirms the significant role of calcium on NOM fouling relative to sodium and magnesium. Error bars, here, represent the standard deviations of three measurements.

In the presence of calcium and magnesium, DOC concentrations and $SUVA_{254}$ values decrease in the feedwater after fouling (Table S4), indicating hydrophobic NOM fouls RO membranes in the presence of divalent cations. NOM molecular weight distributions in the feedwaters shift to lower molecular weights upon fouling in the presence of calcium and magnesium (Figure 1B), confirming the significant contribution of hydrophobic, high molecular weight NOM to divalent cation-induced membrane fouling. In the presence of a monovalent cation, sodium, DOC concentration, $SUVA_{254}$ value, and HPSEC peak position do not significantly change, implying sodium-induced NOM fouling is not specific to NOM of a certain size/hydrophobicity. In the NOM-Na fouling experiment, permeate flux plateaued after approximately 500 L/m^2, but the permeate flux decreased throughout the entire experiment for the hard (i.e., high calcium/magnesium-containing) feedwaters (Figure 1A). This trend suggests NOM-Na fouling occurs via initial adsorption/attachment of NOM to the RO membrane surface, presumably driven by charge neutralization. Meanwhile, divalent cations promote continued growth of fouling layers via bridging of high molecular weight NOM. Bridging of organic foulants can occur in solution and at the membrane surface [22,27]; the inset in Figure 1B shows calcium (but not sodium or magnesium) to aggregate NOM in solution, which likely contributes to the greater flux decline observed for calcium relative to the other cations. In this work, solution-phase NOM-Ca aggregation is hypothesized to be mediated by the membrane surface because no aggregation occurred in aliquots taken from the pre-fouling SNOM-Ca feedwater throughout the same duration as the fouling experiments (Section S1.2). One explanation for this finding is that, as the permeate flux declines during constant pressure experiments using the recirculated feedwaters, the balance between the driving force pulling foulants towards the

membrane surface and the shear force of the crossflow velocity changes, and foulant aggregates are able to detach from the membrane fouling layers and recirculate in the feedwater [56,57]. Moreover, concentration polarization of (in)organic foulants at the membrane/water interface increases the probability for NOM aggregation, which likely plays a role in the dynamic fouling behavior observed in this work.

Significant changes in the organic composition of the hard feedwaters are noted upon fouling, but concentrations of divalent cations in the recirculated feedwaters did not change due to the high ratio of divalent cations to organic functional groups in the feedwaters. Based on the experimental conditions and acid-base titration of the NOM (Figure S3), the feedwaters contained approximately 30 mmol (60 meq) Ca^{2+} or Mg^{2+} per milliequivalent of negative charge in NOM. To this end, accumulation of sodium, magnesium, and calcium in NOM fouling layers is evident (Figure 1C). Sodium densities in the three fouling layers are statistically similar (based on two-sided t-tests with α=0.05), but calcium incorporation in NOM fouling layers is almost an order of magnitude higher than that of magnesium. Given the significant flux decline and shift in NOM molecular weight noted during the NOM-Mg experiment, magnesium appears to bridge high molecular weight NOM, yet the influence of this fouling mechanism is less significant than that of calcium. The high affinity of calcium for NOM functional groups relative to magnesium enables calcium-NOM aggregation in solution and extensive RO membrane fouling [58,59].

3.2. Cation-organic interactions drive membrane fouling behavior

The macroscopic results presented in the previous section confirm a significant role of dominant cations on NOM fouling of polyamide membranes. The remainder of this work focuses

on the molecular-level mechanisms that lead to the observed behavior. This section employs NEXAFS spectroscopy to determine the organic composition of NOM fouling layers.

The transmission mode NEXAFS spectrum of the pristine BW30 membrane near the carbon K-edge (Figure 2A) shows the typical features of a polyamide membrane, with a peak at 285 eV indicative of the 1s to π* transition from the aromatic C=C bond and additional features from other functional groups (e.g., amide, carboxyl) [60]. Meanwhile, the surface-sensitive PEY NEXAFS spectrum of the pristine BW30 membrane shows a lower relative amount of aromatic carbon, accompanied by higher relative contributions from carboxyl (≈288 eV) and O-alkyl (≈289 eV) carbon. Differences in the transmission and PEY NEXAFS spectra of the pristine BW30 membrane are likely due to the proprietary surface coating on the commercial RO membrane. Indeed, features in the PEY NEXAFS spectrum of the BW30 membrane resemble the NEXAFS spectrum of polyvinyl alcohol (Figure S11), a hypothesized surface coating [61,62]. The BW30 membrane is smoother/flatter and more hydrophilic (i.e., its contact angle is lower) than several other commercially-available RO membranes, and its reported O/N ratio determined via x-ray photoelectron spectroscopy is significantly higher than other RO membranes (Table S3) [33,34,56], so the fouling mechanisms observed for this surface-coated membrane could be different from that of other membranes. For example, swelling of hydrophilic surface coatings, as observed previously for the BW30 membrane [32], could limit the extent of foulant-membrane interactions. To this end, direct bridging of foulants to the BW30 membrane likely occurred given the PEY NEXAFS spectrum of the pristine BW30 membrane contains contributions from carboxyl carbon.

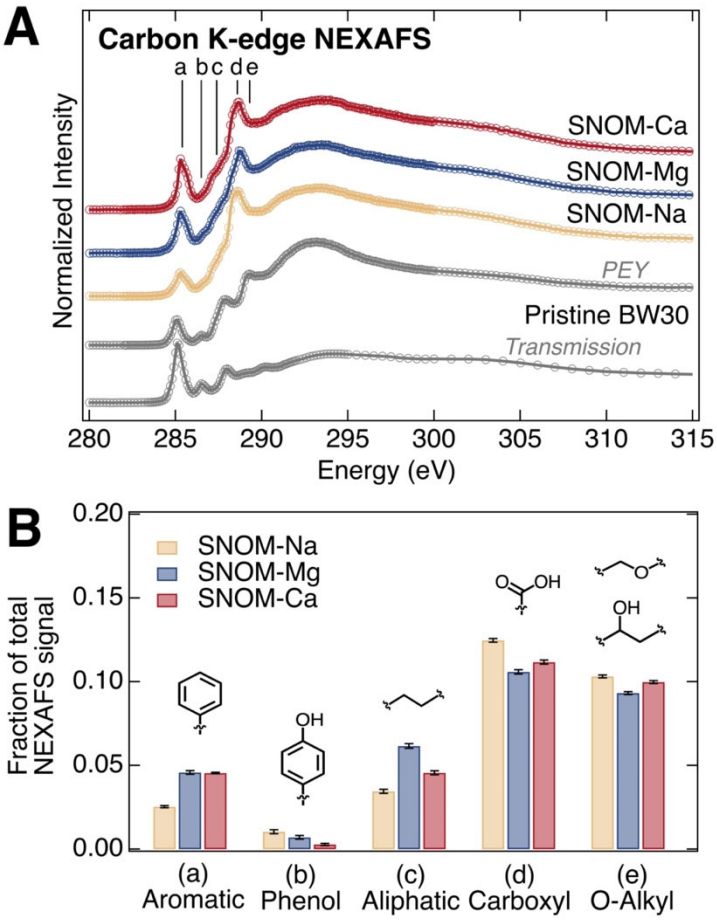

Figure 2. (A) Carbon K-edge NEXAFS spectra of pristine and fouled membranes show clear differences in the organic composition of NOM fouling layers relative to the pristine BW30 membrane. Spectra of the pristine BW30 membrane are presented for data collected using transmission (i.e., transmitting the entire sample thickness) and PEY (surface sensitive) detection modes, while only PEY spectra are shown for NOM-fouled membranes. (B) Fits of carbon K-edge NEXAFS spectra of NOM-fouled membranes to individual components of NOM show divalent cations promote fouling by aromatic/aliphatic-rich NOM and sodium promotes fouling by oxygen-rich NOM (e.g., carboxyl, O-alkyl). Peak assignments are summarized in Table S6 and error bars, here, represent the standard deviations of the fitted area of the Gaussian peaks. Detailed peak fitting results are provided in Section S3.

The PEY NEXAFS spectra of the NOM-fouled membranes near the carbon K-edge are significantly different than that of the pristine membrane, confirming the presence of NOM

fouling layers (Figure 2A). Following the approach of Solomon *et al.* [63,64], deconvolution of the carbon K-edge NEXAFS spectra yields features pertaining to aromatic, phenolic, aliphatic, carboxyl, and O-alkyl carbon (Table S6). Peak assignments are supported by density functional theory predictions of NEXAFS spectra for surrogate compounds (Section S5). Peak fitting results (Figure 2B) show NOM-Ca and NOM-Mg fouling layers contain larger fractions of aromatic and aliphatic carbon and smaller fractions of carboxyl and O-alkyl carbon relative to the NOM-Na fouling layer. This finding supports the solution-phase HPSEC results (Figure 1B) that show divalent cations induce fouling by high molecular weight NOM molecules because larger humic acids generally have lower charge density – and thus, less carboxyl and O-alkyl carbon relative to aliphatic and aromatic carbon – relative to smaller fulvic acids [15]. Indeed, size fractionation of NOM stock solutions using membrane dialysis confirms the higher organic charge density in the low molecular weight fulvic acids present in SNOM and MNOM relative to the higher molecular weight humic acids (Section S1.4). The NOM-Na fouling layer consists of oxygen-rich molecules including polysaccharides and fulvic acids, which can deposit in RO membrane surface cavities [65] and likely contribute to the initial flux decline noted in the NOM-Na experiment. Such fouling is driven by a charge neutralization mechanism [66], while divalent cations cause greater flux decline because, in addition to charge neutralization, they form bridges with high molecular weight NOM.

Peak fitting of the surface sensitive PEY oxygen K-edge NEXAFS spectra of the NOM-fouled membranes corroborate the results at the carbon K-edge, showing the highest carboxyl-oxygen content in the NOM-Ca fouling layer, followed by that of magnesium and then sodium (Figures S15–S17). In other words, carboxyl bridging accounts for majority of the oxygen

present in NOM-Ca fouling layers, whereas electrostatic interactions involving other oxygen-containing functional groups (e.g., alcohols, ethers) contribute more to oxygen accumulation in NOM-Mg and NOM-Na fouling layers. These results highlight the important role of specific (e.g., functional group bridging) and nonspecific (e.g., electrostatic) ion-organic interactions on influencing membrane fouling layer composition. Given the NOM used in these experiments was filtered through 0.22 μm filters, other fouling mechanisms such as hydrophobic adsorption could play a more significant role in unfiltered feedwaters such that the impacts of (non)specific ion-organic interactions that are reported herein would be different for different feedwater chemistries. In addition, membranes with different physiochemical properties (e.g., roughness, surface chemistry) could experience different contributions of individual fouling mechanisms when compared to the BW30 membrane used in this work and they should be considered in future work.

3.3. Calcium aggregates NOM on nanometer length scales

Alongside investigation of the organic composition of NOM fouling layers, further measurements studied the coordination of divalent cations in NOM fouling layers. Sodium was not considered for this investigation because it only forms weak electrostatic complexes with functional groups in NOM [28], so its local binding environment is poorly defined. Similarly, the magnesium K-edge NEXAFS spectrum of the NOM-Mg fouled membrane has a weak signal (Figure S18), possibly due to the low magnesium density in the fouling layer (Figure 1C) and the lack of a well-defined coordination environment, as suggested by others [67].

418 Calcium forms inner sphere complexes with functional groups in NOM [28], so the
419 calcium $L_{3,2}$-edge and K-edge NEXAFS spectra (Figures 3A and 3B, respectively) of the NOM-
420 Ca fouled membrane exhibit well-defined features representative of calcium-carboxyl complexes
421 (Figure S20). Despite the NOM-Ca feedwater being slightly oversaturated with $CaCO_3$
422 (logSI=0.2), no evidence of mineral scaling is observed. Induction times for $CaCO_3$ precipitation
423 are long (i.e., hours to days) at low oversaturation, and aromatic, high molecular weight NOM
424 can inhibit growth of $CaCO_3$ precipitates by adsorbing to $CaCO_3$ surfaces [68–71]. In turn,
425 calcium-induced membrane fouling occurs via carboxyl bridging under the conditions of these
426 experiments.
427

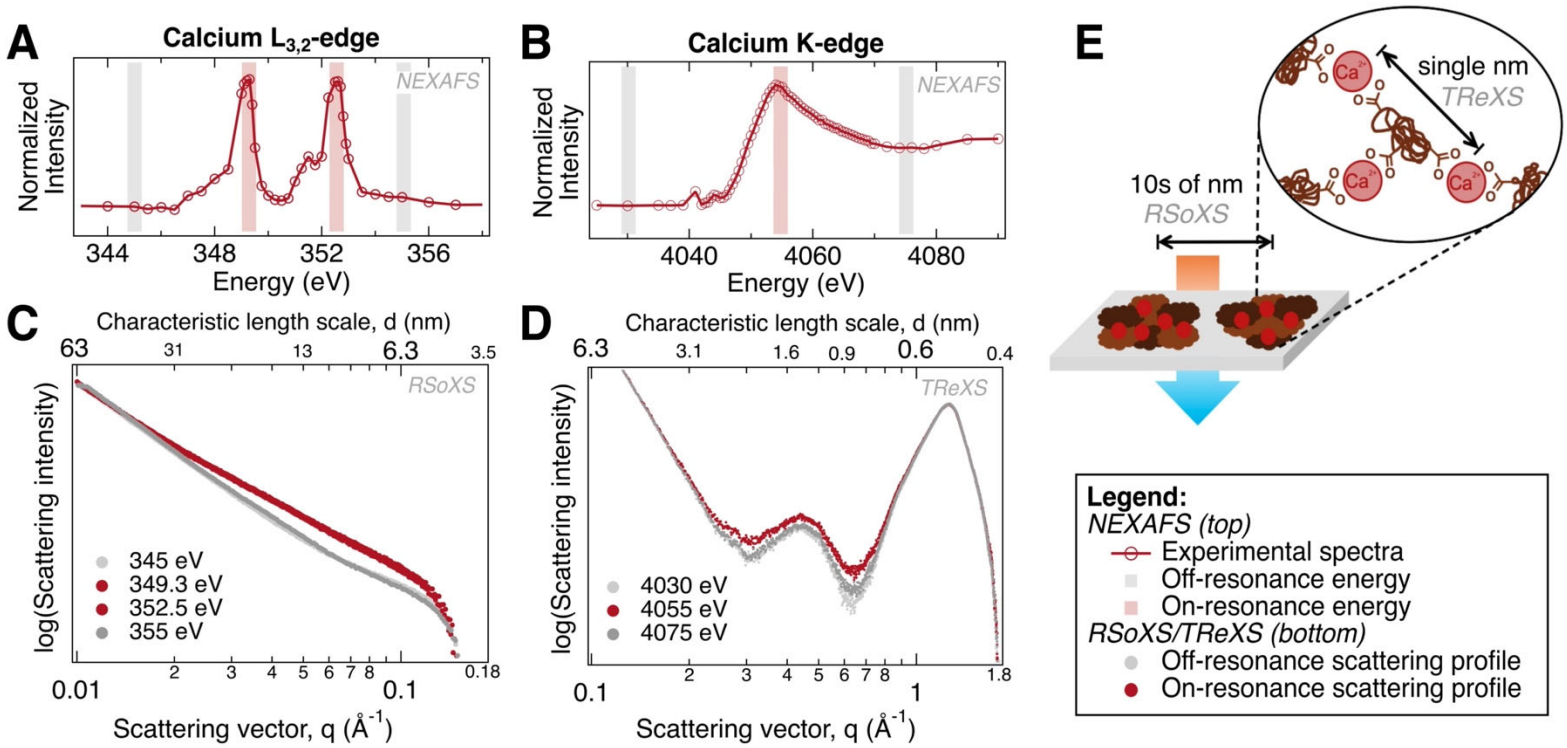

Figure 3. Calcium $L_{3,2}$-edge (A) and K-edge (B) NEXAFS spectra of the NOM-Ca fouled membrane reveal carboxyl bridging as the major fouling mechanism. (C) Ca $L_{3,2}$-edge RSoXS profiles of the NOM-Ca fouled membrane show an enhancement in scattering intensity on-resonance (349.3 eV and 352.5 eV) with characteristic length scales on the order of tens of nanometers. (D) Ca K-edge TReXS profiles also reveal an enhancement in scattering intensity on-resonance at the calcium K-edge (4055 eV), with characteristic length scales on the order of single nanometers. (E) NOM fouling in the presence of calcium occurs via formation of carboxyl-bridged NOM aggregates, promoting a heterogeneous distribution of foulants on the membrane surface.

436 Calcium $L_{3,2}$-edge RSoXS and K-edge TReXS profiles of the NOM-Ca fouled membrane
437 are presented in Figures 3C and 3D, respectively. By tuning the x-ray energy to the calcium
438 absorption edges, increased scattering contrast between calcium and the surrounding sample
439 matrix is achieved (Figures S25 and S27) and the enhanced scattering intensity is attributed to
440 the spacing of calcium atoms/clusters in the samples. These characteristic length scales, d, of
441 calcium domains are inversely proportional to the magnitude of the scattering vector, q ($q=2\pi/d$).
442 The pristine and NOM-Na fouled membranes show no variation in scattering intensity across the
443 calcium absorption edges (Figures S23 and S26). At the calcium $L_{3,2}$-edge, the increase in
444 scattering intensity for the NOM-Ca fouled membrane occurs in the q-range of 0.02 $Å^{-1}$ to
445 0.1 $Å^{-1}$ (Figure 3C), indicative of a characteristic spacing on the order of tens of nanometers.
446 Meanwhile, the enhancement in scattering intensity at the calcium K-edge occurs at q values
447 between 0.2 $Å^{-1}$ and 0.7 $Å^{-1}$ (Figure 3D), representing single nanometer spacing among calcium
448 atoms/clusters within the fouling layers.
449 The difference in characteristic length scales revealed at the calcium absorption edges
450 suggests the shorter (single nanometer) and longer (tens of nanometers) range spacing of
451 calcium-carboxyl complexes within and between NOM aggregates on RO membrane surfaces
452 (Figure 3E). This finding is supported by studies that note similar length scales for the
453 distribution of calcium-carboxyl complexes within (≈2 nm) and between (≈20 nm) microfibril
454 bundles/fibers in plant cell walls [72,73]. Compared to ordered systems such as block
455 copolymers, NOM fouling layers exhibit broad scattering features indicative of relatively
456 disordered matrices; this heterogeneous distribution of membrane foulants is expected given the
457 polydispersity of NOM. Potential remedies for preventing NOM fouling via calcium-induced

458 aggregation include physical instabilities to detach aggregates, chemical addition to break
459 aggregates apart, and membrane modifications (e.g., zwitterionic groups, functional group
460 patterning, tailored roughness) to reduce affinity for aggregate deposition/attachment [74–77].
461 To optimize treatment of specific waters, pretreatment strategies should be tailored to remove
462 those constituents that contribute to significant membrane fouling. For example, hydrophobic
463 NOM can be removed by coagulation/flocculation, oxidation, and sorption [78–80], whereas
464 multivalent cations might require ion exchange and/or electrodialysis pretreatment [43,81,82].
465 Future work on these systems should also investigate the role of other multivalent cations (e.g.,
466 Al^{3+}, Fe^{3+} , Cu^{2+}) that are used during pretreatment and/or present in important water sources
467 (e.g., mining wastewater, oil/gas produced waters) [83–85].
468
469 *3.4. Fouling mechanisms shift in complex waters*
470 As we turn to treating more complex waters for new reuse opportunities, interactions
471 occurring among contaminants must be considered in the design and assessment of treatment
472 processes. In this section, alginate, a model organic foulant with carboxyl groups, and carbonate
473 (CO_3^{2-}), a scale-forming anion, are employed to reveal foulant-foulant interactions that dictate
474 membrane fouling behavior. Alginate fouling was most severe in the presence of calcium (Table
475 S5), and calcite ($\log K_s = -8.4$) is less soluble than magnesite ($\log K_s = -7.5$) [86], so the focus of
476 this section is on calcium-containing feedwaters.
477 Organic fouling by cross-linked calcium alginate is more detrimental to permeate flux
478 compared to $CaCO_3$ scaling alone (Figure 4A). However, as the logSI of calcite in the alginate
479 feedwaters increases from 0.23 (1.7 times the saturation point) to 1.4 (25 times the saturation

480 point), greater flux decline is noted at long operation time (i.e., large permeate volume). The
481 greater flux decline is attributed to the formation of $CaCO_3$ scales on the (fouled) membranes, as
482 seen in the scanning electron micrographs in Figure 4A. WAXS profiles of the fouled
483 membranes (Figure 4B) reveal the presence of calcite and vaterite – two polymorphs of $CaCO_3$ –
484 in the fouling layers with and without alginate. Vaterite, an intermediate phase formed during the
485 crystallization of calcite [87], is present in all the samples, while calcite is only present when
486 logSI>1.0. The induction time for $CaCO_3$ nucleation at logSI values between 0.23 and 1.4 ranges
487 from hours to minutes [68,69,71] and the membrane fouling experiments lasted several hours
488 (Table S5); thus scaling occurs by stable and metastable species.
489

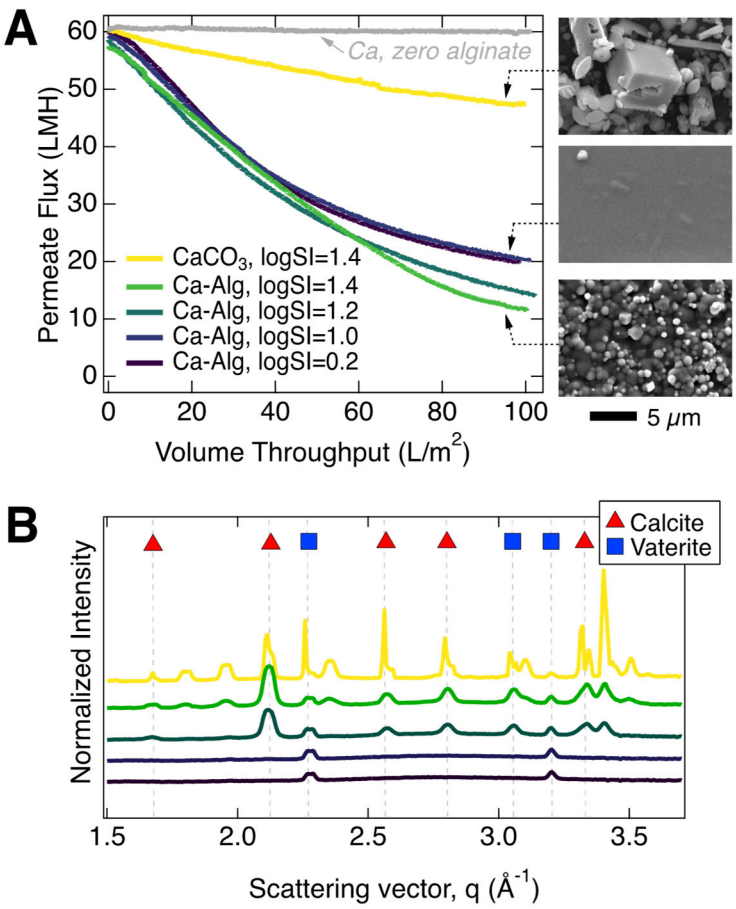

Figure 4. (A) Permeate flux decline is more significant in calcium alginate fouling experiments relative to $CaCO_3$ scaling alone, but $CaCO_3$ incorporation in calcium alginate fouling layers (as seen in the scanning electron micrographs) contributes to greater flux decline at high oversaturation (logSI>1.0). The grey trace confirms that no fouling occurs for the slightly oversaturated (logSI=0.2) feedwater without alginate. (B) WAXS profiles of alginate/$CaCO_3$-fouled membranes reveal vaterite in all the fouling layers and calcite in the fouling layers formed at high $CaCO_3$ oversaturation (logSI>1.0). Peak assignments are based on data reported in literature [88,89].

The transition in fouling mechanism from calcium alginate to $CaCO_3$-embedded calcium-alginate is evident in the calcium K-edge NEXAFS spectra of the membranes (Figure 5A), where the growth of a feature at approximately 4065 eV with increasing logSI is representative of $CaCO_3$ in the fouling layers. Linear combination fits of the NEXAFS spectra (Figure S21) show

calcium alginate accounts for >99 % of calcium fouling at logSI≤1.0, but $CaCO_3$ scaling accounts for 47 % and 57 % of calcium fouling at logSI values of 1.2 and 1.4, respectively. $CaCO_3$ precipitates account for 50 % and 75 % of total calcium in the feedwaters at equilibrium (using relevant constants in the Visual MINTEQ database [90]), suggesting the competing calcium-carboxyl fouling mechanism inhibits/slows the growth of $CaCO_3$ scales on the membrane. Indeed, the flux decline observed for the feedwater that induces both fouling mechanisms (Alg-Ca, logSI=1.4) is less than the sum of the flux declines observed for calcium alginate fouling (Alg-Ca, logSI=0.2) and $CaCO_3$ scaling ($CaCO_3$, logSI=1.4) (Figure S8). Similar behavior has been shown to inhibit the transition of amorphous $CaCO_3$ to calcite in marine organisms and to influence the morphology (i.e., rod-like versus needle-like crystals) of gypsum scales on RO membranes [91–95]. To this end, co-fouling experiments under different conditions (e.g., lower pH, higher concentrations of organic foulants relative to divalent cations) have been show to increase/enhancement mineral scaling [96–98]. This finding has been attributed to increased concentration polarization near the membrane surface in the presence of organic fouling layers and it highlights the multi-faceted nature of fouling phenomena in complex feedwaters. Interestingly, $CaCO_3$ scales appear smaller when alginate is present in the feedwater (Figure 4A), supporting a scaling inhibition mechanism under the conditions of these experiments and encouraging future research. Co-fouling of full- and pilot-scale membranes is frequently reported to include carboxyl-containing organic foulants (e.g., alginate, NOM) and calcium-containing scalants (e.g., calcite, gypsum) [99–104], so future studies should consider the fundamental mechanisms of co-fouling phenenomena in order to design novel pretreatment processes and antifouling membrane materials.

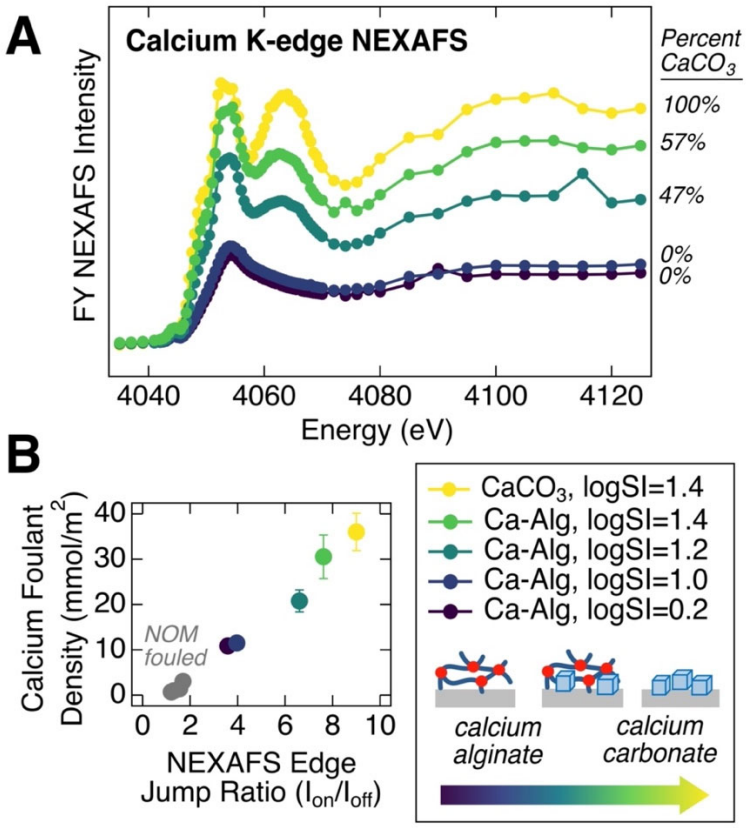

Figure 5. (A) Calcium K-edge NEXAFS spectra of BW30 membranes fouled by calcium alginate at varying $CaCO_3$ oversaturation show the shift in fouling mechanism from cross-linked calcium alginate to $CaCO_3$-embedded calcium alginate fouling layers. The values on the right of the plot present the percent contribution of $CaCO_3$ to the NEXAFS spectra based on linear combination fits. (B) Calcium K-edge jump ratios determined by fluorescence yield NEXAFS spectroscopy shows good agreement (R^2=0.988) with calcium densities in membrane fouling layers determined by microwave digestion/ICP-OES analysis.

Alongside the shift in fouling mechanism is an increase in the calcium K-edge jump (i.e., the difference between the pre- and post-edge NEXAFS intensity), indicating higher concentrations of calcium in the $CaCO_3$-containing fouling layers. This increase is expected based on the higher calcium content of a $CaCO_3$ crystal relative to a calcium alginate compound. A strong linear relationship (R^2=0.988) exists between calcium K-edge jump ratios and calcium

densities in the fouling layers determined macroscopically (Figure 5B). This result highlights the value of advanced characterization techniques such as fluorescence yield NEXAFS spectroscopy to provide detailed, element-specific information – including speciation and quantification – of membranes fouled by complex mixtures. Extension of the multimodal characterization platform presented herein to additional systems, including other foulant mixtures (e.g., sulfate/carbonate, sulfate/NOM, silica/alginate, gypsum/iron oxides [105–109]) and novel materials (e.g., antifouling surface coatings, patterned surfaces [74–76,110,111]), will lead to significant advancements that support the design of novel treatment trains for new reuse opportunities.

4. Conclusions

This work reveals key mechanisms of RO membrane fouling by dominant (in)organic contaminants through a combination of bench-scale membrane fouling expeirments, water quality analyses, and fouling layer characterization. NOM fouling of polyamide membranes in the presence of Na^+ is shown to occur via electrostatic interactions involving fulvic acids and other oxygen-rich molecules, while divalent cations (Ca^{2+} and Mg^{2+}) promote carboxyl bridging of hydrophobic, high molecular weight organic foulants that are more detrimental to membrane flux. Ca^{2+}, but not Mg^{2+}, is shown to aggregate NOM in solution, which leads to the nanoscale aggregation of calcium-carboxyl complexes in NOM fouling layers. Membrane fouling expeirments employing complex feedwaters containing mixtures of calcium, alginate, and carbonate show alginate inhibits/slows the growth of calcite precipitates, and the flux decline observed for the co-fouling mechanism was less significant than the sum of its parts. These results highlight the importance of synergistic/antagonistic mechanisms in the design of future

566 treatment process/material design. Moreover, this study demonstrates the important role of
567 advanced characterization techniques including x-ray absorption spectroscopy and (resonant) x-
568 ray scattering to provide the molecular-level insight that relate fundamental water quality
569 parameters to fouling behavior and overall membrane performance.

Acknowledgements

This work was supported in part through the Center for Materials for Water and Energy Systems (M-WET), an Energy Frontier Research Center funded by the U.S. Department of Energy (DOE), Office of Science, Basic Energy Sciences under Award #DE-SC0019272. This work was supported in part by the Laboratory Directed Research and Development Program of Lawrence Berkeley National Laboratory under U.S. Department of Energy Contract No. DE-AC02-05CH11231. M.R.L. was supported in part by an ALS Collaborative Postdoctoral Fellowship. This research used the Spectroscopy Soft and Tender 1 (SST-1) and the Soft Matter Interfaces (SMI) beamlines of the National Synchrotron Light Source II, a U.S. DOE Office of Science User Facility operated by Brookhaven National Laboratory under Contract #DE-SC0012704. This research used resources of the Advanced Light Source (beamline 7.3.3) and the Molecular Foundry, which are supported by the U.S. DOE Office of Science, Basic Energy Sciences under Contract #DE-AC02-05CH11231. Certain commercial names are used in this manuscript for the purposes of illustration and do not imply recommendation or endorsement by the National Institute of Standards and Technology.

Author contribution statement

M.R.L.: Conceptualization, Investigation, Writing – Original Draft. **S.R.:** Investigation, Writing – Review & Editing. **G.F.:** Investigation, Writing – Review & Editing. **E.G.:** Investigation, Writing – Review & Editing. **C.J.:** Investigation, Writing – Review & Editing. **D.F.L.:** Conceptualization, Investigation, Writing – Review & Editing, Supervision, Funding Acquisition. **L.E.K.:** Conceptualization, Investigation, Writing – Review & Editing,

592 Supervision, Funding Acquisition. **G.M.S.:** Conceptualization, Investigation, Writing – Review

593 & Editing, Supervision, Funding Acquisition.

References

[1] D.M. Warsinger, S. Chakraborty, E.W. Tow, M.H. Plumlee, C. Bellona, S. Loutatidou, L. Karimi, A.M. Mikelonis, A. Achilli, A. Ghassemi, L.P. Padhye, S.A. Snyder, S. Curcio, C.D. Vecitis, H.A. Arafat, J.H. Lienhard, A review of polymeric membranes and processes for potable water reuse, Prog Polym Sci. 81 (2018) 209–237. https://doi.org/10.1016/j.progpolymsci.2018.01.004.

[2] M.R. Landsman, R. Sujanani, S.H. Brodfuehrer, C.M. Cooper, A.G. Darr, R.J. Davis, K. Kim, S. Kum, L.K. Nalley, S.M. Nomaan, C.P. Oden, A. Paspureddi, K.K. Reimund, L.S.R. III, S. Yeo, D.F. Lawler, B.D. Freeman, L.E. Katz, Water treatment: Are membranes the panacea?, Annual Review in Chemical and Biomolecular Engineering. 11 (2020) 1–27. https://doi.org/10.1017/CBO9781107415324.004.

[3] L.F. Greenlee, D.F. Lawler, B.D. Freeman, B. Marrot, P. Moulin, Reverse osmosis desalination: Water sources, technology, and today's challenges, Water Res. 43 (2009) 2317–2348. https://doi.org/10.1016/j.watres.2009.03.010.

[4] A. Matin, T. Laoui, W. Falath, M. Farooque, Fouling control in reverse osmosis for water desalination & reuse: Current practices & emerging environment-friendly technologies, Science of The Total Environment. 765 (2021) 142721. https://doi.org/10.1016/j.scitotenv.2020.142721.

[5] P. Xu, J.E. Drewes, T.U. Kim, C. Bellona, G. Amy, Effect of membrane fouling on transport of organic contaminants in NF/RO membrane applications, J Memb Sci. 279 (2006) 165–175. https://doi.org/10.1016/j.memsci.2005.12.001.

[6] K.L. Tu, A.R. Chivas, L.D. Nghiem, Effects of membrane fouling and scaling on boron rejection by nanofiltration and reverse osmosis membranes, Desalination. 279 (2011) 269–277. https://doi.org/10.1016/j.desal.2011.06.019.

[7] S. Im, H. Lee, H. Rho, The fouling layers characteristics of osmotically driven membranes affect transport behaviors of reverse salt permeation and per-fluorinated compounds, Desalination. 540 (2022) 116001. https://doi.org/10.1016/j.desal.2022.116001.

[8] C. Liu, W. Wang, B. Yang, K. Xiao, H. Zhao, Separation, anti-fouling, and chlorine resistance of the polyamide reverse osmosis membrane: From mechanisms to mitigation strategies, Water Res. 195 (2021) 116976. https://doi.org/10.1016/j.watres.2021.116976.

[9] J. Rolf, T. Cao, X. Huang, C. Boo, Q. Li, M. Elimelech, Inorganic Scaling in Membrane Desalination: Models, Mechanisms, and Characterization Methods, Environ Sci Technol. 56 (2022) 7484–7511. https://doi.org/10.1021/acs.est.2c01858.

[10] Y. Ma, J.W. Chew, Investigation of membrane fouling phenomenon using molecular dynamics simulations: A review, J Memb Sci. 661 (2022) 120874. https://doi.org/10.1016/j.memsci.2022.120874.

[11] F. Tang, H.Y. Hu, L.J. Sun, Y.X. Sun, N. Shi, J.C. Crittenden, Fouling characteristics of reverse osmosis membranes at different positions of a full-scale plant for municipal wastewater reclamation, Water Res. 90 (2016) 329–336. https://doi.org/10.1016/j.watres.2015.12.028.

[12] S. Jiang, Y. Li, B.P. Ladewig, A review of reverse osmosis membrane fouling and control strategies, Science of the Total Environment. 595 (2017) 567–583. https://doi.org/10.1016/j.scitotenv.2017.03.235.

[13] A. Braghetta, F.A. Digiano, W.P. Ball, Nanofiltration of Natural Organic Matter: pH and Ionic Strength Effects, Journal of Environmental Engineering. 123 (1997) 628–641.
[14] S. Hong, M. Elimelech, Chemical and physical aspects of natural organic matter (NOM) fouling of nanofiltration membranes, J Memb Sci. 132 (1997) 159–181. https://doi.org/10.1016/S0376-7388(97)00060-4.
[15] G.R. Aiken, D.M. McKnight, R.L. Wershaw, P. MacCarthy, Humic Substances in Soil, Sediment, and Water: Geochemistry, Isolation, and Characterization, J. Wiley, New York, 1985.
[16] J.D. Ritchie, E. Michael Perdue, Proton-binding study of standard and reference fulvic acids, humic acids, and natural organic matter, Geochim Cosmochim Acta. 67 (2003) 85–96. https://doi.org/10.1016/S0016-7037(02)01044-X.
[17] V. Freger, G.Z. Ramon, Polyamide desalination membranes: Formation, structure, and properties, Prog Polym Sci. 122 (2021) 101451. https://doi.org/10.1016/j.progpolymsci.2021.101451.
[18] W. Stumm, J.J. Morgan, Aquatic Chemistry: Chemical Equilibria and Rates in Natural Waters, 3rd ed., Wiley Interscience, Hoboken, NJ, 1996.
[19] J. Adusei-Gyamfi, B. Ouddane, L. Rietveld, J.P. Cornard, J. Criquet, Natural organic matter-cations complexation and its impact on water treatment: A critical review, Water Res. 160 (2019) 130–147. https://doi.org/10.1016/j.watres.2019.05.064.
[20] W.Y. Ahn, A.G. Kalinichev, M.M. Clark, Effects of background cations on the fouling of polyethersulfone membranes by natural organic matter: Experimental and molecular modeling study, J Memb Sci. 309 (2008) 128–140. https://doi.org/10.1016/j.memsci.2007.10.023.
[21] E. Iskrenova-Tchoukova, A.G. Kalinichev, R. James Kirkpatrick, Metal cation complexation with natural organic matter in aqueous solutions: Molecular dynamics simulations and potentials of mean force, Langmuir. 26 (2020) 15909–15919. https://doi.org/10.1021/la102535n.
[22] F. Xu, Y. Yao, P.J.J. Alvarez, Q. Li, H. Fu, D. Yin, D. Zhu, X. Qu, Specific ion effects on the aggregation behavior of aquatic natural organic matter, J Colloid Interface Sci. 556 (2019) 734–742. https://doi.org/10.1016/j.jcis.2019.09.001.
[23] C.Y. Tang, Y.N. Kwon, J.O. Leckie, Fouling of reverse osmosis and nanofiltration membranes by humic acid-Effects of solution composition and hydrodynamic conditions, J Memb Sci. 290 (2007) 86–94. https://doi.org/10.1016/j.memsci.2006.12.017.
[24] S. Lee, W.S. Ang, M. Elimelech, Fouling of reverse osmosis membranes by hydrophilic organic matter: Implications for water reuse, Desalination. 187 (2006) 313–321. https://doi.org/10.1016/j.desal.2005.04.090.
[25] K. Ghosh, M. Schnitzer, Macromolecular structures of humic substances, Soil Sci. 129 (1980) 266–276. https://doi.org/10.1097/00010694-198005000-00002.
[26] A.E. Childress, M. Elimelech, Effect of solution chemistry on the surface charge of polymeric reverse osmosis and nanofiltration membranes, J Memb Sci. 119 (1996) 253–268. https://doi.org/10.1016/0376-7388(96)00127-5.
[27] Q. Li, M. Elimelech, Organic fouling and chemical cleaning of nanofiltration membranes: Measurements and mechanisms, Environ Sci Technol. 38 (2004) 4683–4693. https://doi.org/10.1021/es0354162.

[28] A.G. Kalinichev, R.J. Kirkpatrick, Molecular dynamics simulation of cationic complexation with natural organic matter, Eur J Soil Sci. 58 (2007) 909–917. https://doi.org/10.1111/j.1365-2389.2007.00929.x.
[29] A. Antony, J.H. Low, S. Gray, A.E. Childress, P. Le-Clech, G. Leslie, Scale formation and control in high pressure membrane water treatment systems: A review, J Memb Sci. 383 (2011) 1–16. https://doi.org/10.1016/j.memsci.2011.08.054.
[30] A.N. Quay, T. Tong, S.M. Hashmi, Y. Zhou, S. Zhao, M. Elimelech, Combined Organic Fouling and Inorganic Scaling in Reverse Osmosis: Role of Protein-Silica Interactions, Environ Sci Technol. 52 (2018) 9145–9153. https://doi.org/10.1021/acs.est.8b02194.
[31] K.G. Lu, M. Li, H. Huang, Silica scaling of reverse osmosis membranes preconditioned by natural organic matter, Science of the Total Environment. 746 (2020) 141178. https://doi.org/10.1016/j.scitotenv.2020.141178.
[32] E. Dražević, K. Košutić, V. Freger, Permeability and selectivity of reverse osmosis membranes: Correlation to swelling revisited, Water Res. 49 (2014) 444–452. https://doi.org/10.1016/j.watres.2013.10.029.
[33] C.Y. Tang, Y.-N. Kwon, J.O. Leckie, Effect of membrane chemistry and coating layer on physiochemical properties of thin film composite polyamide RO and NF membranes, Desalination. 242 (2009) 168–182. https://doi.org/10.1016/j.desal.2008.04.004.
[34] C. TANG, Y. KWON, J. LECKIE, Probing the nano- and micro-scales of reverse osmosis membranes—A comprehensive characterization of physiochemical properties of uncoated and coated membranes by XPS, TEM, ATR-FTIR, and streaming potential measurements, J Memb Sci. 287 (2007) 146–156. https://doi.org/10.1016/j.memsci.2006.10.038.
[35] W. Chen, C. Qian, K.G. Zhou, H.Q. Yu, Molecular Spectroscopic Characterization of Membrane Fouling: A Critical Review, Chem. 4 (2018) 1492–1509. https://doi.org/10.1016/j.chempr.2018.03.011.
[36] S.E. Bone, H.G. Steinrück, M.F. Toney, Advanced Characterization in Clean Water Technologies, Joule. 4 (2020) 1637–1659. https://doi.org/10.1016/j.joule.2020.06.020.
[37] P. Fiske, E.J. Crumlin, Water-Energy Synchrotron Research, Synchrotron Radiat News. 33 (2020) 2. https://doi.org/10.1080/08940886.2020.1784692.
[38] Y.S. Jun, D. Kim, C.W. Neil, Heterogeneous Nucleation and Growth of Nanoparticles at Environmental Interfaces, Acc Chem Res. 49 (2016) 1681–1690. https://doi.org/10.1021/acs.accounts.6b00208.
[39] N.W. Green, D. McInnis, N. Hertkorn, P.A. Maurice, E.M. Perdue, Suwannee River natural organic matter: Isolation of the 2R101N reference sample by reverse osmosis, Environ Eng Sci. 32 (2015) 38–44. https://doi.org/10.1089/ees.2014.0284.
[40] IHSS, IHSS Team collects NOM from the Upper Mississippi River, (n.d.). https://humic-substances.org/ihss-team-collects-nom-from-the-upper-mississippi-river/ (accessed December 31, 2021).
[41] S.M. Serkiz, E.M. Perdue, Isolation of dissolved organic matter from the suwannee river using reverse osmosis, Water Res. 24 (1990) 911–916. https://doi.org/10.1016/0043-1354(90)90142-S.
[42] M.R. Landsman, D.F. Lawler, L.E. Katz, Application of electrodialysis pretreatment to enhance boron removal and reduce fouling during desalination by nanofiltration/reverse osmosis, Desalination. 491 (2020) 114563. https://doi.org/10.1016/j.desal.2020.114563.

[43] S. Kum, M.R. Landsman, G.M. Su, G. Freychet, D.F. Lawler, L.E. Katz, Performance of a Hybrid ED−NF Membrane System for Water Recovery Improvement via NOM Fouling Control, ACS ES&T Engineering. (2021).
[44] J.L. Weishaar, G.R. Aiken, B.A. Bergamaschi, M.S. Fram, R. Fujii, K. Mopper, Evaluation of specific ultraviolet absorbance as an indicator of the chemical composition and reactivity of dissolved organic carbon, Environ Sci Technol. 37 (2003) 4702–4708. https://doi.org/10.1021/es030360x.
[45] B.C. McAdams, G.R. Aiken, D. McKnight, W.A. Arnold, Y.-P. Chin, High Pressure Size Exclusion Chromatography (HPSEC) Determination of Dissolved Organic Matter Molecular Weight Revisited: Accounting for Changes in Stationary Phases, Analytical Standards, and Isolation Methods, Environ Sci Technol. 52 (2018) 722–730.
[46] W.S. Rasband, ImageJ, U. S. National Institute of Health, Bethesda, Maryland, USA, https://imagej.nih.gov/ij/, (1997).
[47] J.M. Virgili, Y. Tao, J.B. Kortright, N.P. Balsara, R.A. Segalman, Analysis of order formation in block copolymer thin films using resonant soft X-ray scattering, Macromolecules. 40 (2007) 2092–2099. https://doi.org/10.1021/ma061734k.
[48] B.A. Collins, E. Gann, Resonant soft X-ray scattering in polymer science, Journal of Polymer Science. (2021) 1–45. https://doi.org/10.1002/pol.20210414.
[49] G.M. Su, I.A. Cordova, C. Wang, New Insights into Water Treatment Materials with Chemically Sensitive Soft and Tender X-rays, Synchrotron Radiat News. 33 (2020) 17–23. https://doi.org/10.1080/08940886.2020.1784695.
[50] E. Gann, T. Crofts, G. Holland, P. Beaucage, T. McAfee, R.J. Kline, B.A. Collins, C.R. McNeill, D.A. Fischer, D.M. DeLongchamp, A NIST facility for resonant soft x-ray scattering measuring nano-scale soft matter structure at NSLS-II, Journal of Physics Condensed Matter. 33 (2020). https://doi.org/10.1088/1361-648X/abdffb.
[51] K.E. Sohn, M.D. Dimitriou, J. Genzer, D.A. Fischer, C.J. Hawker, E.J. Kramer, Determination of the electron escape depth for NEXAFS spectroscopy, Langmuir. 25 (2009) 6341–6348. https://doi.org/10.1021/la803951y.
[52] B.L. Henke, E.M. Gullikson, J.C. Davis, X-ray interactions: Photoabsorption, scattering, transmission, and reflection at E = 50-30, 000 eV, Z = 1-92, At Data Nucl Data Tables. 54 (1993) 181–342. https://doi.org/10.1006/adnd.1993.1013.
[53] T.E. Culp, Y. Shen, M. Geitner, M. Paul, A. Roy, M.J. Behr, S. Rosenberg, J. Gu, M. Kumar, E.D. Gomez, Electron tomography reveals details of the internal microstructure of desalination membranes, Proceedings of the National Academy of Sciences. 115 (2018) 8694–8699. https://doi.org/10.1073/pnas.1804708115.
[54] M. Zhernenkov, N. Canestrari, O. Chubar, E. DiMasi, Soft matter interfaces beamline at NSLS-II: geometrical ray-tracing vs. wavefront propagation simulations, in: M. Sanchez del Rio, O. Chubar (Eds.), 2014: p. 92090G. https://doi.org/10.1117/12.2060889.
[55] A. Hexemer, W. Bras, J. Glossinger, E. Schaible, E. Gann, R. Kirian, A. MacDowell, M. Church, B. Rude, H. Padmore, A SAXS/WAXS/GISAXS Beamline with Multilayer Monochromator, J Phys Conf Ser. 247 (2010) 012007. https://doi.org/10.1088/1742-6596/247/1/012007.

[56] C.Y. Tang, J.O. Leckie, Membrane Independent Limiting Flux for RO and NF Membranes Fouled by Humic Acid, Environ Sci Technol. 41 (2007) 4767–4773. https://doi.org/10.1021/es063105w.
[57] S.P. Palecek, A.L. Zydney, Intermolecular electrostatic interactions and their effect on flux and protein deposition during protein filtration, Biotechnol Prog. 10 (1994) 207–213. https://doi.org/10.1021/bp00026a010.
[58] A.K. Pandey, S.D. Pandey, V. Misra, Stability constants of metal-humic acid complexes and its role in environmental detoxification, Ecotoxicol Environ Saf. 47 (2000) 195–200. https://doi.org/10.1006/eesa.2000.1947.
[59] I. Christl, Magnesium binding by terrestrial humic acids, Environmental Chemistry. 15 (2018) 317–324. https://doi.org/10.1071/EN18084.
[60] T.E. Culp, D. Ye, M. Paul, A. Roy, M.J. Behr, S. Jons, S. Rosenberg, C. Wang, E.W. Gomez, M. Kumar, E.D. Gomez, Probing the Internal Microstructure of Polyamide Thin-Film Composite Membranes Using Resonant Soft X-ray Scattering, ACS Marco Letters. 7 (2018) 927–932.
[61] O. Dhez, H. Ade, S.G. Urquhart, Calibrated NEXAFS spectra of some common polymers, J Electron Spectros Relat Phenomena. 128 (2003) 85–96. https://doi.org/10.1016/S0368-2048(02)00237-2.
[62] C.Y. Tang, Y.N. Kwon, J.O. Leckie, Probing the nano- and micro-scales of reverse osmosis membranes-A comprehensive characterization of physiochemical properties of uncoated and coated membranes by XPS, TEM, ATR-FTIR, and streaming potential measurements, J Memb Sci. 287 (2007) 146–156. https://doi.org/10.1016/j.memsci.2006.10.038.
[63] D. Solomon, J. Lehmann, J. Kinyangi, B. Liang, T. Schäfer, Carbon K-Edge NEXAFS and FTIR-ATR Spectroscopic Investigation of Organic Carbon Speciation in Soils, Soil Science Society of America Journal. 69 (2005) 107–119. https://doi.org/10.2136/sssaj2005.0107dup.
[64] J. Lehmann, D. Solomon, J. Brandes, H. Fleckenstein, C. Jacobsen, J. Thieme, Synchrotron-based near-edge X-ray spectroscopy of natural organic matter in soils and sediments, in: Biophysico-Chemical Processes Involving Natural Nonliving Organic Matter in Environmental Systems, John Wiley & Sons, Inc., 2009. www.lightsources.org.
[65] R. Cruz-silva, Y. Takizawa, A. Nakaruk, M. Katouda, New insights in the natural organic matter fouling mechanism of polyamide and nanocomposite multiwalled carbon nanotubes-polyamide membranes, Environ Sci Technol. (2019). https://doi.org/10.1021/acs.est.8b07203.
[66] S. Lee, M. Elimelech, Relating Organic Fouling of Reverse Osmosis Membranes to Intermolecular Adhesion Forces, Environ Sci Technol. 40 (2006) 980–987. https://doi.org/10.1021/es051825h.
[67] O. Branson, S.A.T. Redfern, T. Tyliszczak, A. Sadekov, G. Langer, K. Kimoto, H. Elderfield, The coordination of Mg in foraminiferal calcite, Earth Planet Sci Lett. 383 (2013) 134–141. https://doi.org/10.1016/j.epsl.2013.09.037.
[68] M.M. Reddy, Effect of magnesium ion on calcium carbonate nucleation and crystal growth in dilute aqueous solutions at 25°C, U.S. Geological Survey Bulletin. 1578 (1986) 169–182.

[69] J.A. Nason, D.F. Lawler, Particle size distribution dynamics during precipitative softening: Constant solution composition, Water Res. 42 (2008) 3667–3676. https://doi.org/10.1016/j.watres.2008.05.016.
[70] Y.P. Lin, P.C. Singer, G.R. Aiken, Inhibition of calcite precipitation by natural organic material: Kinetics, mechanism, and thermodynamics, Environ Sci Technol. 39 (2005) 6420–6428. https://doi.org/10.1021/es050470z.
[71] J.Y. Choi, K.A. Kinney, L.E. Katz, Effect of $CaCO_{3(S)}$ nucleation modes on algae removal from alkaline water, Environ Sci Technol. (2016) acs.est.5b05255. https://doi.org/10.1021/acs.est.5b05255.
[72] S. Rongpipi, Structural characterization of plant cell walls using synchrotron X-ray, 2021.
[73] D. Ye, S.N. Kiemle, S. Rongpipi, X. Wang, C. Wang, D.J. Cosgrove, E.W. Gomez, E.D. Gomez, Resonant soft X-ray scattering reveals cellulose microfibril spacing in plant primary cell walls, Sci Rep. 8 (2018). https://doi.org/10.1038/s41598-018-31024-1.
[74] J.I. Monroe, S. Jiao, R.J. Davis, D. Robinson Brown, L.E. Katz, M.S. Shell, Affinity of small-molecule solutes to hydrophobic, hydrophilic, and chemically patterned interfaces in aqueous solution, Proceedings of the National Academy of Sciences. 118 (2021). https://doi.org/10.1073/pnas.2020205118.
[75] J.R. Werber, C.O. Osuji, M. Elimelech, Materials for next-generation desalination and water purification membranes, Nat Rev Mater. 1 (2016). https://doi.org/10.1038/natrevmats.2016.18.
[76] X. Zhao, R. Zhang, Y. Liu, M. He, Y. Su, C. Gao, Z. Jiang, Antifouling membrane surface construction: Chemistry plays a critical role, J Memb Sci. 551 (2018) 145–171. https://doi.org/10.1016/j.memsci.2018.01.039.
[77] S. Shao, F. Zeng, L. Long, X. Zhu, L.E. Peng, F. Wang, Z. Yang, C.Y. Tang, Nanofiltration Membranes with Crumpled Polyamide Films: A Critical Review on Mechanisms, Performances, and Environmental Applications, Environ Sci Technol. 56 (2022) 12811–12827. https://doi.org/10.1021/acs.est.2c04736.
[78] G.-Q. Chen, Y.-H. Wu, P.-S. Fang, Y. Bai, Z. Chen, Y.-Q. Xu, Y.-H. Wang, X. Tong, L.-W. Luo, H.-B. Wang, Z.-W. Zhang, N. Ikuno, H.-Y. Hu, Performance of different pretreatment methods on alleviating reverse osmosis membrane fouling caused by soluble microbial products, J Memb Sci. 641 (2022) 119850. https://doi.org/10.1016/j.memsci.2021.119850.
[79] W. SONG, Nanofiltration of natural organic matter with H2O2/UV pretreatment: fouling mitigation and membrane surface characterization, J Memb Sci. 241 (2004) 143–160. https://doi.org/10.1016/j.memsci.2004.04.034.
[80] Y. Wan, P. Xie, Z. Wang, J. Wang, J. Ding, R. Dewil, B. Van der Bruggen, Application of UV/chlorine pretreatment for controlling ultrafiltration (UF) membrane fouling caused by different natural organic fractions, Chemosphere. 263 (2021) 127993. https://doi.org/10.1016/j.chemosphere.2020.127993.
[81] A. ABRAHAMSE, C. LIPREAU, S. LI, S. HEIJMAN, Removal of divalent cations reduces fouling of ultrafiltration membranes, J Memb Sci. 323 (2008) 153–158. https://doi.org/10.1016/j.memsci.2008.06.018.

[82] K.A. Indarawis, T.H. Boyer, Evaluation of ion exchange pretreatment options to decrease fouling of a reverse osmosis membrane, Desalination Water Treat. 52 (2014) 4603–4611. https://doi.org/10.1080/19443994.2013.867416.
[83] T. TRAN, B. BOLTO, S. GRAY, M. HOANG, E. OSTARCEVIC, An autopsy study of a fouled reverse osmosis membrane element used in a brackish water treatment plant, Water Res. 41 (2007) 3915–3923. https://doi.org/10.1016/j.watres.2007.06.008.
[84] L. Sun, W. Lin, D. Li, K. Xiao, D. Chen, S. Luo, X. Huang, Significant insights of Cu and Fe as key metals to cause RO membrane fouling under coal-mining wastewater treatment, Desalination. 555 (2023) 116517. https://doi.org/10.1016/j.desal.2023.116517.
[85] Z.-H. Li, G.-W. Ni, J.-L. Wang, L. Zhou, Q. Yang, P.-Z. Li, A.-L. Gao, T. Yu, L.-H. Cheng, X.-J. Bi, Fouling characteristic of reverse osmosis membrane for reclaimed water treatment operating under cold winter condition, Desalination. 549 (2023) 116309. https://doi.org/10.1016/j.desal.2022.116309.
[86] François M. M. Morel, Janet G. Hering, Principles and applications of aquatic chemistry, Wiley, 1993.
[87] P. Bots, L.G. Benning, J.-D. Rodriguez-Blanco, T. Roncal-Herrero, S. Shaw, Mechanistic Insights into the Crystallization of Amorphous Calcium Carbonate (ACC), Cryst Growth Des. 12 (2012) 3806–3814. https://doi.org/10.1021/cg300676b.
[88] M. Liu, G. Gadikota, Phase Evolution and Textural Changes during the Direct Conversion and Storage of CO2 to Produce Calcium Carbonate from Calcium Hydroxide, Geosciences (Basel). 8 (2018) 445. https://doi.org/10.3390/geosciences8120445.
[89] M. Liu, G. Gadikota, Integrated CO2 Capture, Conversion, and Storage To Produce Calcium Carbonate Using an Amine Looping Strategy, Energy & Fuels. 33 (2019) 1722–1733. https://doi.org/10.1021/acs.energyfuels.8b02803.
[90] J.P. Gustafsson, Visual MINTEQ, (2012). https://vminteq.lwr.kth.se/.
[91] J. Aizenberg, L. Addadi, S. Weiner, G. Lambert, Stabilization of amorphous calcium carbonate by specialized macromolecules in biological and synthetic precipitates, Advanced Materials. 8 (1996) 222–226. https://doi.org/10.1002/adma.19960080307.
[92] J. Aizenberg, G. Lambert, S. Weiner, L. Addadi, Factors Involved in the Formation of Amorphous and Crystalline Calcium Carbonate: A Study of an Ascidian Skeleton, J Am Chem Soc. 124 (2002) 32–39. https://doi.org/10.1021/ja016990l.
[93] M. Wang, B. Cao, Y. Hu, D.F. Rodrigues, Mineral Scaling on Reverse Osmosis Membranes: Role of Mass, Orientation, and Crystallinity on Permeability, Environ Sci Technol. 55 (2021) 16110–16119. https://doi.org/10.1021/acs.est.1c04143.
[94] O.N. Karaseva, L.Z. Lakshtanov, D. V. Okhrimenko, D.A. Belova, J. Generosi, S.L.S. Stipp, Biopolymer Control on Calcite Precipitation, Cryst Growth Des. 18 (2018) 2972–2985. https://doi.org/10.1021/acs.cgd.8b00096.
[95] A.J. Giuffre, L.M. Hamm, N. Han, J.J. De Yoreo, P.M. Dove, Polysaccharide chemistry regulates kinetics of calcite nucleation through competition of interfacial energies, Proceedings of the National Academy of Sciences. 110 (2013) 9261–9266. https://doi.org/10.1073/pnas.1222162110.
[96] J. Wang, L. Wang, R. Miao, Y. Lv, X. Wang, X. Meng, R. Yang, X. Zhang, Enhanced gypsum scaling by organic fouling layer on nanofiltration membrane: Characteristics and

mechanisms, Water Res. 91 (2016) 203–213. https://doi.org/10.1016/j.watres.2016.01.019.
[97] J. Thompson, N. Lin, E. Lyster, R. Arbel, T. Knoell, J. Gilron, Y. Cohen, RO membrane mineral scaling in the presence of a biofilm, J Memb Sci. 415–416 (2012) 181–191. https://doi.org/10.1016/j.memsci.2012.04.051.
[98] A. Karanasiou, A.J. Karabelas, S.T. Mitrouli, Incipient membrane scaling in the presence of polysaccharides during reverse osmosis desalination in spacer-filled channels, Desalination. 500 (2021) 114821. https://doi.org/10.1016/j.desal.2020.114821.
[99] A. Antony, N. Subhi, R.K. Henderson, S.J. Khan, R.M. Stuetz, P. Le-Clech, V. Chen, G. Leslie, Comparison of reverse osmosis membrane fouling profiles from Australian water recycling plants, J Memb Sci. 407–408 (2012) 8–16. https://doi.org/10.1016/j.memsci.2012.02.039.
[100] L. Zheng, D. Yu, G. Wang, Z. Yue, C. Zhang, Y. Wang, J. Zhang, J. Wang, G. Liang, Y. Wei, Characteristics and formation mechanism of membrane fouling in a full-scale RO wastewater reclamation process: Membrane autopsy and fouling characterization, J Memb Sci. 563 (2018) 843–856. https://doi.org/10.1016/j.memsci.2018.06.043.
[101] B. Abada, J. Safarik, K.P. Ishida, S. Chellam, Elucidating Foulant Diversity during Full-Scale Potable Reuse: Forensic Analysis of Lead and Lag Elements of a Three-Stage Reverse Osmosis System, ACS ES&T Engineering. 2 (2022) 2116–2129. https://doi.org/10.1021/acsestengg.2c00171.
[102] P. Xu, C. Bellona, J.E. Drewes, Fouling of nanofiltration and reverse osmosis membranes during municipal wastewater reclamation: Membrane autopsy results from pilot-scale investigations, J Memb Sci. 353 (2010) 111–121. https://doi.org/10.1016/j.memsci.2010.02.037.
[103] B. Abada, J. Safarik, K.P. Ishida, S. Chellam, Surface characterization of end-of-life reverse osmosis membranes from a full-scale advanced water reuse facility: Combined role of bioorganic materials and silicon on chemically irreversible fouling, J Memb Sci. 653 (2022) 120511. https://doi.org/10.1016/j.memsci.2022.120511.
[104] F. Tang, H.-Y. Hu, L.-J. Sun, Y.-X. Sun, N. Shi, J.C. Crittenden, Fouling characteristics of reverse osmosis membranes at different positions of a full-scale plant for municipal wastewater reclamation, Water Res. 90 (2016) 329–336. https://doi.org/10.1016/j.watres.2015.12.028.
[105] Y. Zhu, Q. Li, D. Kim, Y. Min, B. Lee, Y.-S. Jun, Sulfate-Controlled Heterogeneous $CaCO_3$ Nucleation and Its Non-linear Interfacial Energy Evolution, Environ Sci Technol. 55 (2021) 11455–11464. https://doi.org/10.1021/acs.est.1c02865.
[106] T. Cao, J. Rolf, Z. Wang, C. Violet, M. Elimelech, Distinct impacts of natural organic matter and colloidal particles on gypsum crystallization, Water Res. 218 (2022) 118500. https://doi.org/10.1016/j.watres.2022.118500.
[107] D. Li, W. Lin, R. Shao, Y.-X. Shen, X. Zhu, X. Huang, Interaction between humic acid and silica in reverse osmosis membrane fouling process: A spectroscopic and molecular dynamics insight, Water Res. 206 (2021) 117773. https://doi.org/10.1016/j.watres.2021.117773.

[108] E. Melliti, B. Van der Bruggen, H. Elfil, Combined iron oxides and gypsum fouling of reverse osmosis membranes during desalination process, J Memb Sci. 653 (2022) 120472. https://doi.org/10.1016/j.memsci.2022.120472.
[109] T.P. Pham Le, M.S. Jouini, A. Al Masri Alwan, S. Agashichev, M. AlSuwaidi, E. Alhseinat, Optical coherence tomography and digital image processing for scaling and Co-precipitation investigation on reverse osmosis membrane, J Memb Sci. (2023) 121658. https://doi.org/10.1016/j.memsci.2023.121658.
[110] S. Das, M.G. O'Connell, H. Xu, R. Bernstein, J.-H. Kim, K. Sankhala, T. Segal-Peretz, R. Shevate, W. Zhang, X. Zhou, S.B. Darling, J.B. Dunn, Assessing Advances in Anti-fouling Membranes to Improve Process Economics and Sustainability of Water Treatment, ACS ES&T Engineering. (2022). https://doi.org/10.1021/acsestengg.2c00184.
[111] X. Zhao, R. Zhang, Y. Liu, M. He, Y. Su, C. Gao, Z. Jiang, Antifouling membrane surface construction: Chemistry plays a critical role, J Memb Sci. 551 (2018) 145–171. https://doi.org/10.1016/j.memsci.2018.01.039.